ADVANCED FUNCTIONAL MATERIALS
www.afm-journal.de

Spatiotemporally Controlled Access to Photoluminescence Dark State of 2D Monolayer Semiconductor by FRAP Microscopy

Hua Su, Yufeng Nie, Qianlu Sun, Linliang Yin, Jian Li, Xing-Hua Xia, Weigao Xu, and Wei Wang**

Tailoring the photoluminescence (PL) of semiconductors through spatiotemporal manipulation of dynamics of photoexcited carriers is of paramount importance for understanding the emitting mechanism and developing high-performance devices. Herein, fluorescence recovery after photobleaching (FRAP) microscopy, a powerful tool in biology, is first utilized to simultaneously manipulate and monitor the dynamics of photoexcited carrier in attractive 2D transition metal dichalcogenide monolayers (1L-TMDs). This allows on-demand access to the PL dark state of 1L-TMDs, based on the triggered exciton–exciton annihilation by pump beam-initiated photodoping. Using a 0.7-µm-diametered pump laser, the PL dark region can be facilely tailored from ≈0.5 to ≈5 µm over a 10-µm-1L-WS_2 flake. An interesting photoinduced dedoping effect in 1L-TMDs after photodoping is discovered by FRAP, which has not been observed before and might account for the non-blinking emission of 1L-TMDs. The revealed mono-exponential photo-dedoping can also be kinetically tailored by ≈170-fold (k: 0.11–19.00 s^{-1}) by humidity, power of incident laser and type of 1L-TMDs. This study demonstrates the power of FRAP microscopy in exploring the effect of photoexcited carrier dynamics on the PL property of semiconductors, holding promises for understanding light-emitting mechanism and optimizing operational parameters for optoelectronic devices.

1. Introduction

Upon light illumination, photoexcited charge carriers (electron–hole pair, so-called exciton) generate in semiconductors, and the subsequent radiative recombination of these carriers can generate light emission.[1,2] Reducing the dimension of bulk semiconductor to nanoscale brings about significant quantum confinement effect, and unprecedently boosts the quantum yield (QY) of photoluminescence (PL), such as the scenario of colloidal quantum dots (QDs).[1,2] Extremely promoted by the QDs, semiconductor-based luminescent materials have achieved tremendous progresses from controlled synthesis to manipulation of their optical properties over the last 30 years, and shown promising applications in photodetectors, light-emitting devices, biological imaging, and so on.[2–5] While the outstanding optical property of these emitters due to the nanoscale confinement effect, interactions among photoexcited carriers and effect of structural defects on photophysical process are concomitantly prominent in these low-dimensional nanostructures.[6,7] This sometimes gives rise to unwanted PL property, such as the PL dark state in QDs (i.e., a decreased PLQY attributed to non-radiative Auger recombination of charge carriers caused by surface structural defects).[6–12] Therefore, elucidating the impact of photoexcited charge carrier dynamics on the PL properties of semiconductor is of paramount importance for understanding the underlying emitting mechanism and developing high-performance optoelectronic devices; in this sense, it is highly desirable to spatiotemporally manipulate and visually monitor the dynamics of photoexcited carriers.

Since 2010, three-atom-thick transition metal dichalcogenide monolayers (1L-TMDs), with the general chemical formula of MX_2 (M = Mo, W and X = S, Se), a large lateral size up to tens of microns and a near-unity PLQY, has newly emerged as an attractive 2D semiconductor for optoelectronic device application and fundamental solid-state physics research.[13–23] Compared to the traditional semiconductors, 1L-TMDs possess several impressive features. First, external stimuli-sensitive X-M-X sandwich structure of 1L-TMDs, manifests itself versatile in engineering the PL property through modulating the intrinsic/photoexcited charge carriers and their interactions over the whole flake, by virtue of molecule adsorption (H_2O, O_2, organic molecule, etc.),[24–27] electric control[18,28] and light stimulation.[29–35] Second, 1L-TMDs possess higher exciton binding energy (tens of meV to hundreds of meV), owing to the atomic layer-thin spatial confinement and reduced Coulomb screening

H. Su, J. Li, X.-H. Xia, W. Wang
State Key Laboratory of Analytical Chemistry for Life Science
School of Chemistry and Chemical Engineering
Nanjing University
Nanjing 210023, China
E-mail: wei.wang@nju.edu.cn
Y. Nie, Q. Sun, W. Xu
Key Laboratory of Mesoscopic Chemistry
School of Chemistry and Chemical Engineering
Nanjing University
Nanjing 210023, China
E-mail: xuwg@nju.edu.cn
L. Yin
Olympus (China) Co., Ltd.
Shanghai 200031, China

The ORCID identification number(s) for the author(s) of this article can be found under https://doi.org/10.1002/adfm.202107551.

DOI: 10.1002/adfm.202107551

effect.[15,36] The enhanced electrostatic interaction between electron and hole also leads to a much stronger exciton–exciton interaction in 1L-TMDs compared to other semiconductors.[33,37,38] For instance, 1L-TMDs possess a highly effective exciton–exciton annihilation (EEA) at an exciton density of ≈10^{10} cm^{-2} (corresponding to an inter-exciton distance of ≈100 nm), in which one exciton recombines non-radiatively and transfers its energy to another exciton (an excitonic analog of the Auger process in QDs).[33,37–41] This usually leads to a decreased PLQY with increasing power of incident light.[16] The long diffusion distance of neutral exciton in 2D 1L-TMDs (even up to 1.5 μm),[42] also contributes the strengthened EEA process,[38] and enabled an effective Auger recombination.[37,43] Moreover, the strong Coulomb interaction for excitons in 1L-TMDs also energetically favors the formation of charged trion species (two electrons and a hole, or two holes and an electron) even at room temperature when a neutral exciton encounters another electron or hole.[40,44,45] Third, atomic defects are relatively rich in 1L-TMDs, especially chalcogen vacancies,[18,25,27,30,37,38,44,46–48] might increase the possibilities of trapping ionized charge carriers from exciton dissociation and promote the Auger-related process,[49] similar to that in single-walled carbon nanotubes (SWCNTs) which possess similar quantum confinement effect and exciton binding energy of hundreds of meV.[50,51] Taking these unique features of 2D 1L-TMDs into consideration, we expected that 2D 1L-TMDs were an ideal platform to explore the effect of the dynamics of photoexcited carrier on the PL property of semiconductor if combining local manipulation of charge carrier concentration and visual widefield PL imaging. Relatively non-blinking emission (i.e., the random PL intensity switching of a single emitter between "ON" and "OFF" state) in most 2D 1L-TMDs,[17,52] also endows it a stable PL background for monitoring the dynamics of photoexcited carriers upon an external carrier injection, such as photodoping.[53,54]

Herein, we developed a two-laser beam technology to on-demand access to the PL dark state of 2D 1L-TMDs in a temporally- and spatially-controlled manner. This was based on the increased EEA effect upon instantaneous injection of abundant excitons via spatiotemporally-controlled high-power pump beam stimulation (photodoping). The widefield PL imaging via a continuous illumination of a low-power probe beam allowed us to decipher a photoactivated dedoping process in 1L-TMDs after the instantaneous photodoping, which has not been observed in 2D 1L-TMDs yet, to the best of our knowledge. Our results further showed the photoassissted dedoping process in 2D 1L-TMDs exhibited a typical monoexponential behavior. Further, the kinetics of this dedoping process can also be facilely tuned by humidity, power density of incident light and type of 1L-TMDs, enabling the 1L-TMDs as excellent models to understand and manipulate the dynamics of photoexcited charge carriers and to further tune the emissive property of 2D 1L-TMDs. Noted that, such two-laser beam configuration is popular in cell biology, also known as fluorescence recovery after photobleaching (FRAP), which has been proven to be a powerful tool to spatiotemporally investigate the mobility of fluorophore-labeled biomolecules of interest within the cells.[55–57] Through photobleaching the region of interest (ROI) and monitoring the subsequent molecular diffusion-induced PL recovery profile, the binding properties and transport dynamics of particular biomolecules can be unveiled.[55–57] Despite the similarity in optical configuration, this study represents the first attempt to adopt the FRAP concept to spatiotemporally manipulate and monitor the dynamics of photoexcited carrier in 2D semiconductor.

2. Results and Discussion

Considering the exciton density of 2D 1L-TMDs can be easily tailored by the power density of excitation light,[37,39,58] we utilized the commercially available FRAP microscope (based on an Olympus IX-83 microscope) to spatiotemporally manipulate and visually monitor the dynamics of photoexcited carrier in 1L-TMDs, with the principle shown in **Figure 1**A. Briefly, a low-power continuous-wave (CW) probe laser beam (488 nm, with a spot size of ≈100 μm in diameter, ≈5 W cm^{-2}) was continuously illuminated onto a flake of 1L-TMD through an oil-immersed objective lens for wide-field recording the PL signals of the 1L-TMD. At a certain timepoint, a tightly-focused Gaussian-like CW high-power laser (405 nm, with a spot size of ≈0.7 μm in diameter) was utilized as a pump beam (with a pulse width of 3–30 ms) to locally trigger the enhanced EEA effect in the 1L-TMD via instantaneous injection of abundant excitons. After the dramatical disturbance, the PL behavior of the 1L-TMD was continuously monitored with a fast imaging camera (29.4–62.5 frames per second), until reaching the equilibrium state. 2D 1L-WS_2 was first chosen as the model in this study, due to its high PL quantum yield at room temperature as compared to those of other 1L-TMDs.[40,59] The 1L-WS_2 was mechanically exfoliated from a bulk WS_2 crystal according to our previous work,[17] and characterized by bright-field/PL/Raman measurement (Figure S1, Supporting Information) and atomic force microscopy (AFM) (Figure S2, Supporting Information).

Before FRAP experiment, we first checked the effect of power density of incident light on the PL emission of the as-prepared 1L-WS_2 (Figure S3, Supporting Information), and found that the PL intensity of 1L-WS_2 scaled nonlinearly with the exciation power of the 488-nm laser above ≈30 W cm^{-2}. This threshhod predicted an enhanced EEA effect in our sample if further increasing the excitation power.[16] Therefore, for the 488-nm probe laser, a slightly lower power denstiy of ≈5 W cm^{-2} was usually used, thus generating an estimated exciton density of ≈4.88×10^{8} cm^{-2}. While for the 405-nm pump laser, a much higher excitation power in the range of ≈1.6–142.8 kW cm^{-2} was utilized to locally inject abundant excitons in 1L-TMDs, thus corresponding to an inter-exciton distance of 17.6 –1.9 nm (with an estimated excition density of 3.27×10^{11}–2.9×10^{13} cm^{-2}). This distance is significantly shorter than that of diffusion length of excitons in 1L-TMDs and potentially beneficial for the exciton-exciton annihilation process,[38] while still larger than the reported exciton Bohr radius ≈1 nm.[58] The estimation of exciton density was based on the assumption that one absorbed photon generated one exciton,[34,37,39,49] and the detailed calculation was presented in the section 2 of the supporting information.

The top panels in Figure 1B presents the selected time-lapsed PL images of a 1L-WS_2 flake with a lateral size of ≈10 μm. Before a 405-nm pump stimulation ($t < 0$), the PL intensity of 1L-WS_2 just shows a slight fluctuation (initial state, marked by a gray

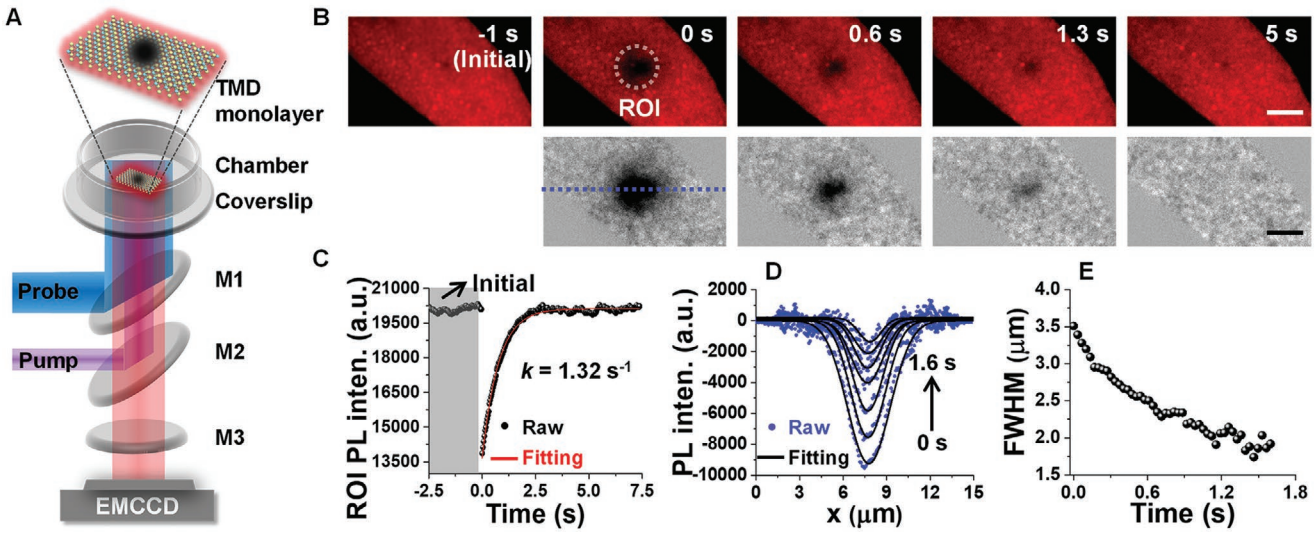

Figure 1. Access to the PL dark state of 2D 1L-WS_2 via a two-laser beam technology. A) Schematic illustration of the FRAP microscope for manipulating and monitoring the PL dark state of a flake of 1L-TMD placed in a temperature- and moisture-controlled chamber. A high-power continous-wave (CW) pump laser beam (405 nm, ≈0.7 μm diameter) was tightly focused onto the flake to trigger the PL dark state through photodoping, and another continuously-illuminated low-power CW probe beam (488 nm, ≈100 μm diameter) was introduced for wide-field imaging of the dedoping process. M1, M2, and M3 are optical filters. An electron-multiplying charge-coupled device (EMCCD) was equipped to sensitively record the wide-field PL images at an imaging acquisition rate up to 29.4 frames per second. B) Selected time-lapsed PL images of a 1L-WS_2 during a typical PL recovery process. Upon a 30-ms pulse stimulation, a PL dark region appeared (t = 0 s), followed by a slow recovery to the bright state. For each image in the PL recovery, the initial state image was subtracted to show the PL dark region clearly. Scale bar: 3 μm. C) The time-dependent PL intensity averaged over a given circular ROI (marked by the white dashed line in (B) shows a mono-exponential recovery kinetics after the pump stimulation, with a recovery rate (k) of 1.32 s^{-1}. D) Time-evolved PL intensity profile along the blue dashed line illustrated in (B) after the stimulation, and corresponding fitting results using a Gaussian function. E) Evolution of full width at half maximum (FWHM) as a function of time during the PL recovery. Parameters of two incident lasers: 405-nm laser, 0.2 mW (≈40.8 kW cm^{-2}), 30-ms pump time; 488-nm laser, 3 mW, ≈5 W cm^{-2}.

color in Figure 1C). Upon a 30-ms pump stimulation, a PL dark region immediately appeared near the point of stimulation, followed by a gradual recovery to the bright state upon the continuous illumination of a 488-nm probe beam in a timescale of several seconds. To clearly show the PL dark region, each PL image recorded during PL recovery was subtracted by the initial state image (pre-bleached), as presented in the bottom panels of Figure 1B. The averaged PL intensity trajectory for a given circular ROI (marked by a white dashed line on the top panel of Figure 1B) as a function of time is shown in Figure 1C and Movie S1 (Supporting Information). The PL recovery process followed a typical mono-exponential behavior, with a recovery rate (k) of 1.32 s^{-1}. It should be noted that the PL dark state with a timescale of several seconds was not the lifetime of the exciton-related species in the 1L-TMD, which was generally accepted in the timescale of ≈ps to ≈ns.[16,34,40,41] It should be noted that similar FRAP phenomenon were recently reported in perovskite single crystals, but exhibited a much longer recovery time in the timescale of > 1 h due to totally different mechanism, i.e., photoinduced defect formation from chemical decomposition and closed chemical cycle-induced self-healing effect.[60]

Spatial information of PL dark region during the PL recovery was further extracted from the differential images with the pre-bleached images subtracted (bottom panels of Figure 1B). As presented in Figure 1D, the time-lapsed PL profiles along the blue dashed line (illustrated in the bottom panel of Figure 1B) can be fitted by the Gaussian function PL (t) ∝ exp (-(x-c)^2/2w^2). The obtained temporal evolution of full width at half maximum (FWHM, ≈2.355 w) is shown in Figure 1E. Intriguingly, the FWHM value declined with time as the PL of 1L-WS_2 recovered. This was quite different from that of biofilm system-based FRAP experiment, which usually displays a time-dependent broadened FWHM due to the diffusion of bleached molecules out of the bleached region and/or surrounding non-bleached molecules into the bleached region.[55,61] This suggested that the observed PL bleaching–recovery phenomenon herein had a different mechanism. In addition, quantitative analysis further revealed that the typical FWHM of PL dark region after the 405-nm laser stimulation was much bigger than that of the 405-nm laser (3.5 μm vs 0.7 μm, Figure S4, Supporting Information) and showed a 1.4-μm broadening in comparison with that of 405-nm laser. Although this value was quite close to the reported 1.5-μm diffusion length of neutral exciton in 1L-TMDs, it can't be simply attributed to the exciton diffusion-promoted EEA-induced PL quenching.[38,42] This was because the laser intensity in the tail beyond the FWHM of the 405-nm pump beam was also strong enough to cause the PL quenching of 1L-WS_2, which was evidenced by the observed PL quenching when placing the laser spot 1-μm away from the flake (Figure S5, Supporting Information).

Actually, the PL bleaching–recovery process was highly reversible and repeatable, as shown in **Figure 2**A, indicating that the intactness of 1L-WS_2 retained after the 405-nm laser treatment.[38] It was reported that the reversible adsorption and desorption of gas molecule such as O_2 and H_2O, can also increase or diminish the PL intensity of 1L-WS_2, through

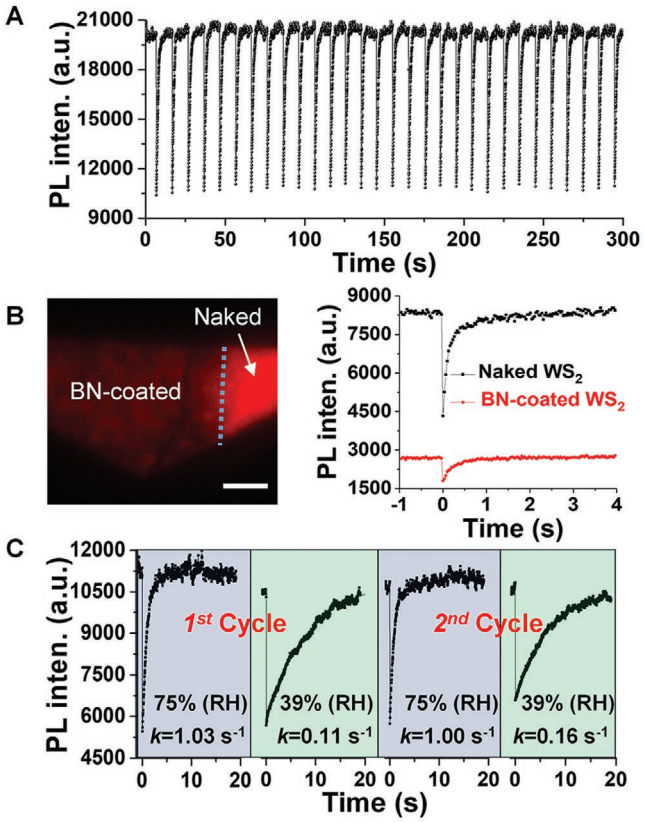

Figure 2. Controllable access to the PL dark state of 2D 1L-WS_2. A) Highly repeatable PL recovery behavior of 2D 1L-WS_2 upon a sequence of 30-ms pulse irradiation using a CW 405-nm pump beam (0.2 mW, ≈40.8 kW cm^{-2}) probed by a CW 488-nm laser (3 mW, ≈5 W cm^{-2}) at room temperature and ambient condition. B) Effect of a flat hexagonal-BN (*h*-BN) film-coating on the PL bleaching–recovery behavior of a flake of 1L-WS_2. The similar phenomena took place on both *h*-BN-coated and -uncoated 1L-WS_2, while a ≈70% decrease in PL intensity occurs on the former condition. Parameters of pump and probe beams were same as that in (A) except for a 10-ms pump time. Scale bar: 2 µm. C) Effect of relative humidity (RH) on the recovery profile of 1L-WS_2 on the condition of fixed concentration of oxygen gas. A remarkably prolonged recovery time was observed in the low RH level (39%), relative to that in high RH level (*k*: 1.00–1.03 s^{-1} vs 0.11–0.16 s^{-1}). The RH level was switched over two cycles for the same 1L-WS_2 flake. Parameters of pump and probe beams were same as that in (B).

decreasing or boosting the charge carrier density of 1L-WS_2, respectively.[26,27] Thus, we partially coated a flake of 1L-WS_2 with a flat hexagonal-BN (*h*-BN) film and performed the same experiment (Figure 2B). As expected, a decrease in PL intensity by ≈70% on *h*-BN-coated 1L-WS_2 compared with that of pristine flake, which was attributed to the increased free electron density owing to the isolation of the monolayer from the air, and thus validated the effective coating. Consequently, similar PL bleaching–recovery kinetics occurred on *h*-BN-coated and -uncoated 1L-WS_2, possibly excluding the photoinduced desorption effect proposed previously.[31] In fact, gas adsorption/desorption usually leads to a slower PL change of 1L-TMDs.[24,26] Further, the effect of relative humidity (RH) on the recovery process of 1L-WS_2 was explored at high RH (75%) and low RH (39%) for two cycles (Figure 2C). Interestingly, the 1L-WS_2 showed a significantly slower recovery rate in the low RH atmosphere, compared with that in high RH level (*k*: 1.03 s^{-1} vs 0.11 s^{-1}). Actually, a slightly higher initial PL intensity appeared in the high RH relative to that of low RH, indicating the passivation of H_2O on the sulfur vacancies of 1L-WS_2. This result is reminiscent of the fact that surface passivation significantly inhibits the PL dark state of QDs, which decreased the trapping possibilities of ionized/ejected carriers by the surface defects in QDs through organic ligand- or inorganic shell-coating.[7,8]

To gain an insight into the bleaching–recovery mechanism, we first explored the possible structural change during the PL bleaching–recovery process via in situ Raman measurement at a time resolution of 0.1s (Figure S6, Supporting Information), and found that no remarkable changes in Raman spectra (including peak position and integrated intensity) occurred to 1L-WS_2. This excluded possible structural changes such as defect formation or phase change,[62,63] and suggested a photophysical mechanism for the observed FRAP behavior. Furthermore, we performed an in situ measurement on the PL spectra of a 1L-WS_2 during the bleaching–recovery process. A slightly slower recovery kinetics (*k*: 0.31 s^{-1}) was intentionally tailored through RH level control to explore the spectral evolution, thus balancing the spectral sensitivity and resolution (top panel of **Figure 3**C). Upon a 473-nm pump laser stimulation, a shoulder PL peak instantaneously appeared on the low-energy side of the main peak, followed by an asymptotical decay to the initial state, as indicated in Figure 3A. The obtained spectra can be fitted by a Voigt function (a convolution of Gaussian and Lorentzian function) to two typical peaks (Figure 3B),[48,64] in which the peaks at ≈2.02 eV and ≈1.97 eV can be assigned to neutral exciton (X^0) and trion (X^-), respectively.[27,29,33,65] A small X^- peak in the initial state of WS_2 possibly resulted from the unintentional *n*-doping due to chalcogen vacancies, which were general structural defects in TMD monolayers exfoliated from commercial crystals.[18,25,27,30,37,38,44,46–48] Low temperature PL mapping also confirmed the existence of plenty of structural defects in the as-exfoliated 1L-WS_2 (Figure S7, Supporting Information). It should be noted that the peak position of X^0 and X^- showed negligible shifts during the whole process, further indicating that the atomic and energy band structure of 1L-WS_2 kept stable in the process,[29] and possibly excluding the pump laser beam-induced thermal effect in our case.[32,34] The integrated PL intensity ratio of X^- to X^0 increased sharply at $t = 0$ s and decayed rapidly during the following PL recovery process (approximately from 0.7 to 0.25, bottom panel of Figure 3C). This confirmed the immediate formation of trions upon the pump laser illumination and subsequent conversion of trions to the neutral excitons. Considering that trion formation requires the existence of excess charge carrier, abundant trions that instantaneously formed suggested a photodoping-triggered free carrier formation by the high-power pump beam excitation (>1 kW cm^{-2}). These can be understood that under the high exciton density (for instance, 3.27×10^{11}–2.9×10^{13} cm^{-2} upon the 405-nm laser pump illumination mentioned above), enhanced exciton–exciton collision and screened Coulomb interactions among excitons promoted the fomation of ionized carriers through exciton dissociation (i.e., Auger ionization).[50,51] Similar trion formation owing to exciton dissociation at high excitation condition has also been observed in SWCNTs

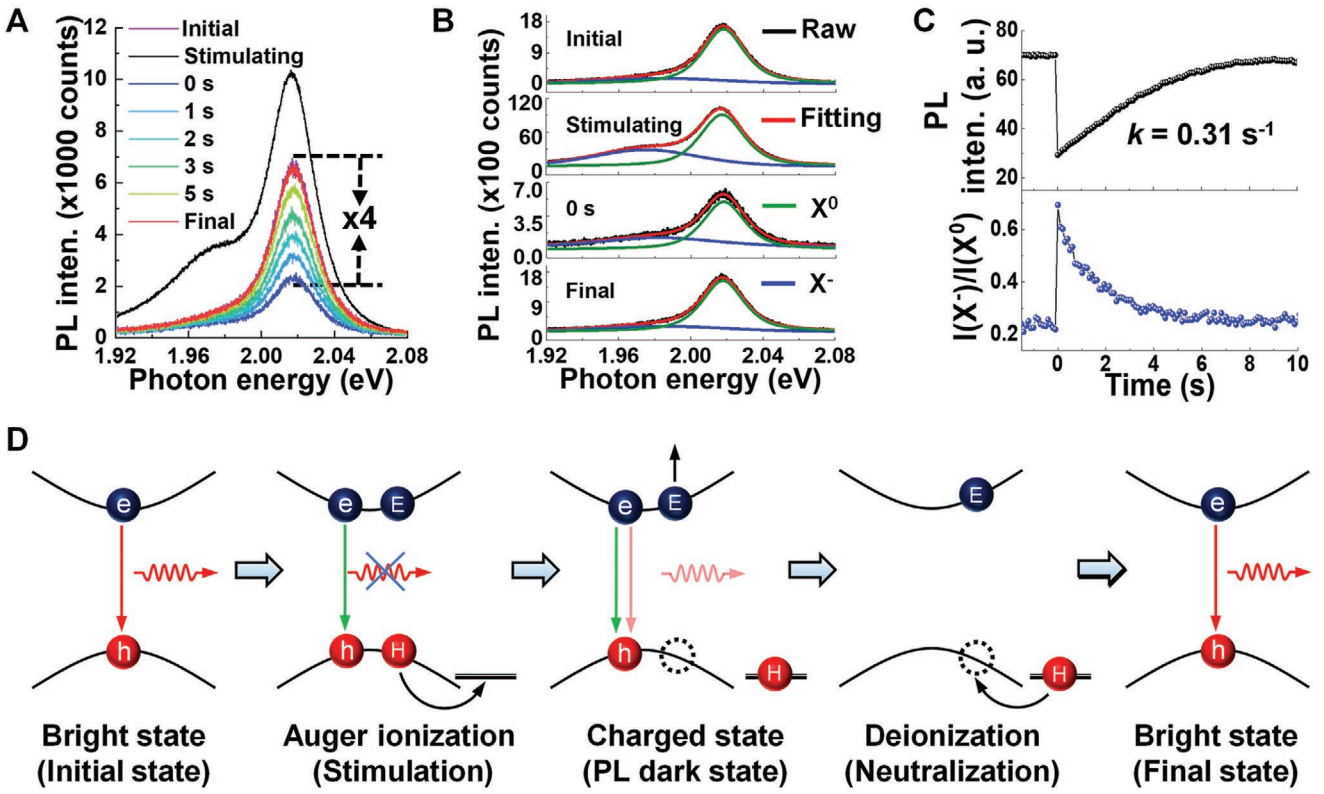

Figure 3. Revealing the underlying mechanism of PL dark state via in situ PL spectroscopic measurement of the 1L-WS_2 flake during the bleaching–recovery process. A) Time-resolved PL spectra of the 1L-WS_2 for a fixed ROI region. A 473-nm CW laser (208.0 μW, ≈20.8 kW cm^{-2}, a ≈500-ms pump time) and a 532-nm CW laser (10.2 μW, ≈1 kW cm^{-2}) were used as the pump beam and probe beam, respectively. Higher PL signals and a shoulder peak on the low-energy side of the main peak appeared upon the pump beam stimulation, while other spectra were magnified by fourfold for clarity. B) Quantitative fitting of the typical spectra with a Voigt function. Two typical peaks can be clearly assigned, which correspond to the neutral exciton (X^0, ≈2.02 eV) and trion (X^-, ≈1.97 eV). C) Time-dependent PL intensity trajectory of the 1L-WS_2 and corresponding integrated PL intensity ratio of X^- to X^0 ($I(X^-)/I(X^0)$), clearly showing a correlation between decay of X^- and PL recovery. D) A proposed model to account for the observed PL bleaching–recovery process, involving initial bright state (low-power irradiation of probe beam), Auger ionization and trapping of charge carrier by surface defects (enhanced exciton–exciton collision caused by instantaneous injection of abundant exciton via a pulse stimulation), charged state, deionization, as well as the re-equilibrium state (neutral state of 1L-WS_2). Red and green arrow show the radiative and non-radiative recombination, respectively. Pale red arrow represents the weakly-emissive process, such as the trion emission.

via transient absorption measurement, which possess similar quantum confinement effect and exciton binding energy of hundreds of meV compared with 1L-TMDs,[50,51] and also proposed for WS_2 monolayer.[49]

Furthermore, we measured the time-evolved PL lifetime based on a time-correlated single photon counting (TCSPC) for the PL bleaching–recovery process (Figure S8, Supporting Information). It was found that the averaged lifetime of 1L-WS_2 was shortened to ≈350 ps for the PL dark state followed by an asymptotic recovery to the initial ≈440 ps, indicating the generation of a new non-radiative recombination pathway triggered by the pump beam stimulation. The nearly synchronized evolution of the PL lifetime with the recorded PL intensity trajectory was much similar to that of trion emission during the in situ PL spectral measurement (Figure 3C), further suggesting the formation of metastable emitting species (trions) during the PL dark state.

Another important aspect is how to understand the several second-timescale recovery kinetics for the triggered PL dark state within 1L-WS_2. This timescale was much longer than that reported recovery time of ≈5 μs in SWCNTs.[51] Generally speaking, the characteristic timescale for the trapped carriers to return into the core of semiconductor is related to the distribution of trap depth of surface defects.[51] In QDs, ms–s timescale charged state is usually observed, which is widely attributed to the heterogeneously-distributed trap depth.[7] 1L-WS_2 is a 2D system (like an ensemble of QDs), which allows for multiple-exciton generation upon photoexcitation and multiple charge carriers trapped by the surface defect sites. The heterogeneity in trap depth for these defects (similar to that of QDs), might cause a random release of these trapped holes, thus leading to a several second-timescale kinetics of PL recovery.

Based on the above experimental results, a photophysical model is proposed in Figure 3D to describe the observed PL bleaching–recovery process. Before the pump beam stimulation (initial state), only a low density of excitons (mainly X^0) generate within the 1L-WS_2 upon the illumination of the low-power probe beam. At a certain timepoint, an illumination of high-power pump laser instantaneously injects abundant excitons in 1L-WS_2. Owing to the high exciton binding energy and long diffusion distance of neutral excitons in 2D 1L-TMDs, a significantly increased EEA process occurs and leads to Auger

ionization (exciton dissociation). The ionized holes are subsequently captured by the rich surface trap sites (sulfur vacancies), thus resulting in an increased density of electrons within the 1L-WS_2 (photodoping effect) and promoting the formation of trions. Thereafter, a remarkable non-radiative Auger recombination occurs by transferring the electron–hole recombination energy into secondary electron of the trion and very weak radiative emission of trion appears,[42,66] hence incurring an apparent PL intensity decrease in the pump beam-stimulated region, i.e., charged state or charge-separated state. On the other hand, upon the continuous illumination of 488-nm laser, the trapped holes are gradually released to neutralize the remaining electrons within 1L-WS_2 through a photoactivation process (described in the following section), accompanied by the reduced density of X^-. When the trapped holes fully recombine with the remaining electrons, the PL of 1L-WS_2 recovers to the initial level. In this mechanism, the PL dark state is the charged state induced by photodoping, and the trion is a by-product during the charging process when a neutral exciton encounters a remaining electron within 1L-WS_2, which can be used as an indicator of the charging process. It should be noted that although this Auger ionization mechanism has been previously proposed in SWCNTs[50,51] and QDs,[7,8,10] we herein first captured the photoactivated deionization process in 1L-TMDs, to the best of our knowledge.

Compared to traditional low-dimensional quantum system, such as QDs and quantum nanowires/nanorods, 2D 1L-TMDs with a large lateral size provide a convenience to explore the photodoping and dedoping process in an accessible temporal and spatial-resolved manner.[34,35,38] We first manipulated the photodoping process by varying the pump power of 405-nm laser across a broad range from 8 to 700 μW, while fixing the duration time of pump irradiation and the parameters of 488-nm probe beam. An irreversible damage of 1L-WS_2 occurred upon the laser stimulation with a power of > 800 μW (data not shown). When the power of 405-nm laser was lower than 8 μW, the charged state of the 1L-WS_2 was below the present detection level. A further increase of the power up to 8 μW would lead to a detectable and reversible PL bleaching–recovery cycle. As indicated in **Figure 4**A, a more obvious PL perturbation was introduced as the pump power increased, that is, a more remarkable decrease in PL intensity. At the power of ≈600 μW, the decrease of PL intensity tended to a saturation, suggesting that all the surface trap sites on the 1L-WS_2 were occupied by the holes ejected during Auger ionization. This point was further supported by the observation that the recovery rate reached a plateau at the power of ≈600 μW (Figure 4B). A slower PL recovery rate was observed at the higher-power stimulation, due to the higher density of trapped holes. Quantitative image analysis further revealed the spatial information with respect to the charged state, i.e., a broaden FWHM value (t = 0 s) upon a higher-power laser stimulation (Figure 4B). A saturated FWHM of ≈4 μm also appeared at ≈600 μW, which was nearly the half size of the measured flake of 1L-WS_2 (≈10 μm).

In order to figure out the role of probe beam irradiation in the dedoping process, the power of 488-nm laser was also altered while fixing the parameters of 405-nm pump laser. As displayed in Figure 4C, the PL recovery profile of 1L-WS_2 under the increased power of 488-nm laser is reasonably

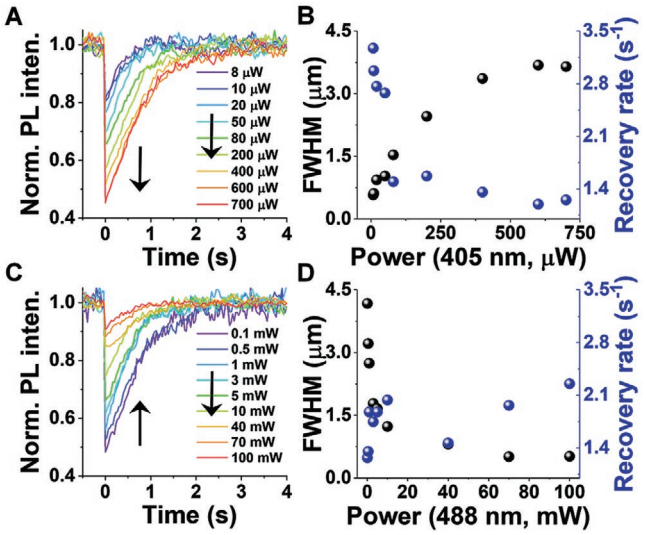

Figure 4. Manipulating the PL dark state of 1L-WS_2 via altering power density of pump beam (405-nm CW laser, 3-ms pump) and probe beam (488-nm CW laser). A, B) Tuning the PL bleaching–recovery process of 1L-WS_2 via altering the power density of pump beam across a broad range from 8 to 700 μW (≈1.6–142.8 kW cm^{-2}). With increasing power of the pump beam, a more obvious PL perturbation, increased FWHM (t = 0 s) and a more sluggish recovery were observed. C, D) Probe beam power-dependent photoinduced dedoping process of 1L-WS_2 in the range of 0.1 to 100 mW (≈0.17–166.7 W cm^{-2}). With increasing power of the probe beam, 1L-WS_2 showed a decreased FWHM (t = 0 s) and a boosted recovery rate.

inverse to that observed for 405-nm laser. As the power of 488-nm laser increased, 1L-WS_2 showed a smaller decline in PL intensity but a boosted recovery rate after bleaching (Figure 4D), clearly showing a photoinduced dedoping effect. This possibly suggested that the release of the trapped holes was facilitated by the photoactivation of 488-nm laser. The photoinduced dedoping effect was further confirmed by the power dependence of the FWHM value, which was also obtained by analyzing a sequence of PL images at t = 0 s. As shown in Figure 4D, the FWHM decreased dramatically as the power of 488-nm laser increased in the case of <10 mW, and tended to level up subsequently. This can be understood that in our experiment, the 405-laser was an approximately Gaussian-shaped beam (Figure S4, Supporting Information), thus leading to a relatively higher density of holes trapped in the central region illuminated and a relatively stable FWHM of ≈0.5 μm. Therefore, a reversibly PL dark region with a FWHM in the range of ≈0.5 to ≈5 μm (half of the lateral size of 1L-WS_2) can be accessed for a 10-μm-sized flake. It should be noted that although photodoping effect has been widely reported in literatures,[29,31,32] such a photoinduced dedoping effect has not been observed in 2D 1L-TMDs, to the best of our knowledge. This means that although rich chalcogen vacancies might trap the photogenerated charge carriers to leading to a PL quenching during the emitting 2D 1L-TMDs, the trapped carriers can indeed be released by the exciting light, therefore creating a relatively equilibrium charge state. This might account for the relatively non-blinking emission of 2D 1L-TMDs in the commonly-used exciting power of ≈W cm^{-2}.[17,52]

Besides *n*-type WS_2, similar PL bleaching–recovery behavior with a typical recovery rate of 19.00 s^{-1} (Figure S9, Supporting Information) and high reversibility (Figure S10, Supporting Information) was also observed for a 2D 1L-WSe_2 flake under the comparable experiment parameters, indicative of the generality of our FRAP microscopy-based method in spatiotemporally-controlled manipulation and monitoring of the dynamics of photoexcited carriers upon an external carrier injection, such as photodoping in 2D 1L-TMDs.

3. Conclusions

In summary, we demonstrated the power of FRAP microscopy to spatiotemporally manipulate and visually monitor the dynamics of photoexcited carrier in 2D monolayer semiconductor for the first time. This enabled us to on-demand access to the PL dark state of 2D 1L-TMDs in a highly reversible and repeated manner, based on the increased EEA effect upon high power of pump beam stimulation (photodoping). Spatially, the PL dark region can be tailored in the range from ≈0.5 to ≈5 µm for a 10-µm flake of 1L-WS_2 upon a pump laser illumination with a 0.7-µm diameter. This was benefit from the large lateral size and high exciton binding energy of atomically thin 1L-TMDs, which strengthened the EEA process upon high-power excitation. The widefield PL imaging upon the continuously-illuminated of probe beam also allowed us to clearly monitor the photoinduced dedoping effect in 1L-TMDs after a spatiotemporally-controlled instantaneous photodoping, which has not been observed in 2D 1L-TMDs yet, to the best of our knowledge. This meant that although rich chalcogen vacancies might trap the photogenerated charge carriers to leading to a PL quenching within 2D 1L-TMDs, the trapped carriers can also be released by the exciting light. This might account for the relatively non-blinking emission of 2D 1L-TMDs in the commonly-used exciting power of ≈W cm^{-2}. Our results further showed that this photoinduced dedoping process exhibited a typically mono-exponential behavior in 2D 1L-TMDs, and the kinetics can be facilely tailored by ≈170 fold (k: 0.11–19.00 s^{-1}) by virtue of humidity, power density of incident laser and type of 1L-TMDs. A photophysical model, i.e., Auger ionization under the enhanced EEA effect and subsequent photoinduced deionization, is plausibly proposed, based on the in situ PL, Raman and lifetime measurements on the bleaching–recovery process. This study demonstrated the atomically thin 2D 1L-TMDs as an excellent model system to explore the effect of the dynamics of photoexcited carrier on the PL property of semiconductors using the powerful FRAP microscopy. We expect that the exact mechanism of exciton dissocation-involved Auger ionization and photoinduced deionization in 2D 1L-TMDs can be further unveiled in future, utilizing an electrostatic force microscopy in conjugation with the easily-tailored structural defects. We believe that manipulation and monitoring of the dynamics of photoexcited carriers will facilitate the understanding of the light emission mechanism and mandatory operational parameter, such as native carrier/environmental factor and excitation conditions, which is pivotal for developing high-performance semiconductor optoelectronic devices.

Supporting Information

Supporting Information is available from the Wiley Online Library or from the author.

Acknowledgements

H.S. and Y.N. contributed equally to this work. The authors acknowledge the financial support from the National Natural Science Foundation of China (Grants 21925403, 21874070, 21873048, 22004066), the Natural Science Foundation of Jiangsu Province (BK20180319, BK20190280), the Fundamental Research Funds for the Central Universities (14380231), and the Excellent Research Program of Nanjing University (Grant ZYJH004).

Conflict of Interest

The authors declare no conflict of interest.

Data Availability Statement

The data that support the findings of this study are available from the corresponding author upon reasonable request.

Keywords

2D monolayer semiconductors, exciton–exciton annihilation, fluorescence imaging, FRAP microscopy, spatiotemporal manipulation

Received: August 2, 2021
Revised: October 24, 2021
Published online:

[1] A. P. Alivisatos, *Science* **1996**, *271*, 933.
[2] C. R. Kagan, E. Lifshitz, E. H. Sargent, D. V. Talapin, *Science* **2016**, *353*, aac5523.
[3] L. H. Manger, M. B. Rowley, Y. Fu, A. K. Foote, M. T. Rea, S. L. Wood, S. Jin, J. C. Wright, R. H. Goldsmith, *J. Phys. Chem. C* **2017**, *121*, 1062.
[4] A. L. Efros, J. B. Delehanty, A. L. Huston, I. L. Medintz, M. Barbic, T. D. Harris, *Nat. Nanotechnol.* **2018**, *13*, 278.
[5] M. Gerhard, B. Louis, R. Camacho, A. Merdasa, J. Li, A. Kiligaridis, A. Dobrovolsky, J. Hofkens, I. G. Scheblykin, *Nat. Commun.* **2019**, *10*, 1698.
[6] P. A. Frantsuzov, S. Volkán-Kacsó, B. Jankó, *Nano Lett.* **2013**, *13*, 402.
[7] A. L. Efros, D. J. Nesbitt, *Nat. Nanotechnol.* **2016**, *11*, 661.
[8] M. Nirmal, B. O. Dabbousi, M. G. Bawendi, J. J. Macklin, J. K. Trautman, T. D. Harris, L. E. Brus, *Nature* **1996**, *383*, 802.
[9] A. L. Efros, M. Rosen, *Phys. Rev. Lett.* **1997**, *78*, 1110.
[10] P. Frantsuzov, M. Kuno, B. Jankó, R. A. Marcus, *Nat. Phys.* **2008**, *4*, 519.
[11] C. Galland, Y. Ghosh, A. Steinbrück, M. Sykora, J. A. Hollingsworth, V. I. Klimov, H. Htoon, *Nature* **2011**, *479*, 203.
[12] X. Hou, J. Kang, H. Qin, X. Chen, J. Ma, J. Zhou, L. Chen, L. Wang, L.-W. Wang, X. Peng, *Nat. Commun.* **2019**, *10*, 1750.
[13] K. F. Mak, C. Lee, J. Hone, J. Shan, T. F. Heinz, *Phys. Rev. Lett.* **2010**, *105*, 136805.
[14] A. Splendiani, L. Sun, Y. Zhang, T. Li, J. Kim, C.-Y. Chim, G. Galli, F. Wang, *Nano Lett.* **2010**, *10*, 1271.
[15] Q. H. Wang, K. Kalantar-Zadeh, A. Kis, J. N. Coleman, M. S. Strano, *Nat. Nanotechnol.* **2012**, *7*, 699.

[16] M. Amani, D.-H. Lien, D. Kiriya, J. Xiao, A. Azcatl, J. Noh, S. R. Madhvapathy, R. Addou, S. KC, M. Dubey, K. Cho, R. M. Wallace, S.-C. Lee, J.-H. He, J. W. Ager, X. Zhang, E. Yablonovitch, A. Javey, *Science* **2015**, *350*, 1065.
[17] W. Xu, W. Liu, J. F. Schmidt, W. Zhao, X. Lu, T. Raab, C. Diederichs, W. Gao, D. V. Seletskiy, Q. Xiong, *Nature* **2017**, *541*, 62.
[18] D.-H. Lien, S. Z. Uddin, M. Yeh, M. Amani, H. Kim, J. W. Ager, E. Yablonovitch, A. Javey, *Science* **2019**, *364*, 468.
[19] Y. Guo, P.-C. Shen, C. Su, A.-Y. Lu, M. Hempel, Y. Han, Q. Ji, Y. Lin, E. Shi, E. McVay, L. Dou, D. A. Muller, T. Palacios, J. Li, X. Ling, J. Kong, *Proc. Natl. Acad. Sci. USA* **2019**, *116*, 3437.
[20] H. Kim, S. Z. Uddin, N. Higashitarumizu, E. Rabani, A. Javey, *Science* **2021**, *373*, 448.
[21] Q. Zhang, Z. Chang, G. Xu, Z. Wang, Y. Zhang, Z.-Q. Xu, S. Chen, Q. Bao, J. Z. Liu, Y.-W. Mai, W. Duan, M. S. Fuhrer, C. Zheng, *Adv. Funct. Mater.* **2016**, *26*, 8707.
[22] Y.-C. Lin, S. Li, H.-P. Komsa, L.-J. Chang, A. V. Krasheninnikov, G. Eda, K. Suenaga, *Adv. Funct. Mater.* **2018**, *28*, 1704210.
[23] J. P. Thiruraman, P. Masih Das, M. Drndić, *Adv. Funct. Mater.* **2019**, *29*, 1904668.
[24] F. K. Perkins, A. L. Friedman, E. Cobas, P. M. Campbell, G. G. Jernigan, B. T. Jonker, *Nano Lett.* **2013**, *13*, 668.
[25] S. Mouri, Y. Miyauchi, K. Matsuda, *Nano Lett.* **2013**, *13*, 5944.
[26] S. Tongay, J. Zhou, C. Ataca, J. Liu, J. S. Kang, T. S. Matthews, L. You, J. Li, J. C. Grossman, J. Wu, *Nano Lett.* **2013**, *13*, 2831.
[27] N. Peimyoo, W. Yang, J. Shang, X. Shen, Y. Wang, T. Yu, *ACS Nano* **2014**, *8*, 11320.
[28] J. S. Ross, S. Wu, H. Yu, N. J. Ghimire, A. M. Jones, G. Aivazian, J. Yan, D. G. Mandrus, D. Xiao, W. Yao, X. Xu, *Nat. Commun.* **2013**, *4*, 1474.
[29] A. A. Mitioglu, P. Plochocka, J. N. Jadczak, W. Escoffier, G. L. J. A. Rikken, L. Kulyuk, D. K. Maude, *Phys. Rev. B* **2013**, *88*, 245403.
[30] J. Lu, A. Carvalho, X. K. Chan, H. Liu, B. Liu, E. S. Tok, K. P. Loh, A. H. Castro Neto, C. H. Sow, *Nano Lett.* **2015**, *15*, 3524.
[31] M. Currie, A. T. Hanbicki, G. Kioseoglou, B. T. Jonker, *Appl. Phys. Lett.* **2015**, *106*, 201907.
[32] F. Cadiz, C. Robert, G. Wang, W. Kong, X. Fan, M. Blei, D. Lagarde, M. Gay, M. Manca, T. Taniguchi, K. Watanabe, T. Amand, X. Marie, P. Renucci, S. Tongay, B. Urbaszek, *2D Mater.* **2016**, *3*, 045008.
[33] Y. Lee, G. Ghimire, S. Roy, Y. Kim, C. Seo, A. K. Sood, J. I. Jang, J. Kim, *ACS Photonics* **2018**, *5*, 2904.
[34] M. Kulig, J. Zipfel, P. Nagler, S. Blanter, C. Schüller, T. Korn, N. Paradiso, M. M. Glazov, A. Chernikov, *Phys. Rev. Lett.* **2018**, *120*, 207401.
[35] P. Qi, Y. Luo, W. Li, Y. Cheng, H. Shan, X. Wang, Z. Liu, P. M. Ajayan, J. Lou, Y. Hou, K. Liu, Z. Fang, *ACS Nano* **2020**, *14*, 6897.
[36] G. Wang, A. Chernikov, M. M. Glazov, T. F. Heinz, X. Marie, T. Amand, B. Urbaszek, *Rev. Mod. Phys.* **2018**, *90*, 021001.
[37] D. Sun, Y. Rao, G. A. Reider, G. Chen, Y. You, L. Brézin, A. R. Harutyunyan, T. F. Heinz, *Nano Lett.* **2014**, *14*, 5625.
[38] S. Mouri, Y. Miyauchi, M. Toh, W. Zhao, G. Eda, K. Matsuda, *Phys. Rev. B* **2014**, *90*, 155449.
[39] N. Kumar, Q. Cui, F. Ceballos, D. He, Y. Wang, H. Zhao, *Phys. Rev. B* **2014**, *89*, 125427.
[40] L. Yuan, L. Huang, *Nanoscale* **2015**, *7*, 7402.
[41] Y. Yu, Y. Yu, C. Xu, A. Barrette, K. Gundogdu, L. Cao, *Phys. Rev. B* **2016**, *93*, 201111.
[42] S. Z. Uddin, H. Kim, M. Lorenzon, M. Yeh, D.-H. Lien, E. S. Barnard, H. Htoon, A. Weber-Bargioni, A. Javey, *ACS Nano* **2020**, *14*, 13433.
[43] L. Li, M.-F. Lin, X. Zhang, A. Britz, A. Krishnamoorthy, R. Ma, R. K. Kalia, A. Nakano, P. Vashishta, P. Ajayan, M. C. Hoffmann, D. M. Fritz, U. Bergmann, O. V. Prezhdo, *Nano Lett.* **2019**, *19*, 6078.
[44] K. F. Mak, K. He, C. Lee, G. H. Lee, J. Hone, T. F. Heinz, J. Shan, *Nat. Mater.* **2013**, *12*, 207.
[45] A. Singh, G. Moody, K. Tran, M. E. Scott, V. Overbeck, G. Berghäuser, J. Schaibley, E. J. Seifert, D. Pleskot, N. M. Gabor, J. Yan, D. G. Mandrus, M. Richter, E. Malic, X. Xu, X. Li, *Phys. Rev. B* **2016**, *93*, 041401.
[46] W. Zhou, X. Zou, S. Najmaei, Z. Liu, Y. Shi, J. Kong, J. Lou, P. M. Ajayan, B. I. Yakobson, J.-C. Idrobo, *Nano Lett.* **2013**, *13*, 2615.
[47] Y. Liu, P. Stradins, S.-H. Wei, *Angew. Chem., Int. Ed.* **2016**, *55*, 965.
[48] O. A. Ajayi, J. V. Ardelean, G. D. Shepard, J. Wang, A. Antony, T. Taniguchi, K. Watanabe, T. F. Heinz, S. Strauf, X. Y. Zhu, J. C. Hone, *2D Mater.* **2017**, *4*, 031011.
[49] A. Boulesbaa, B. Huang, K. Wang, M.-W. Lin, M. Mahjouri-Samani, C. Rouleau, K. Xiao, M. Yoon, B. Sumpter, A. Puretzky, D. Geohegan, *Phys. Rev. B* **2015**, *92*, 115443.
[50] S. M. Santos, B. Yuma, S. Berciaud, J. Shaver, M. Gallart, P. Gilliot, L. Cognet, B. Lounis, *Phys. Rev. Lett.* **2011**, *107*, 187401.
[51] B. Yuma, S. Berciaud, J. Besbas, J. Shaver, S. Santos, S. Ghosh, R. B. Weisman, L. Cognet, M. Gallart, M. Ziegler, B. Hönerlage, B. Lounis, P. Gilliot, *Phys. Rev. B* **2013**, *87*, 205412.
[52] N. Peimyoo, J. Shang, C. Cong, X. Shen, X. Wu, E. K. L. Yeow, T. Yu, *ACS Nano* **2013**, *7*, 10985.
[53] J. Quereda, T. S. Ghiasi, C. H. van der Wal, B. J. van Wees, *2D Mater.* **2019**, *6*, 025040.
[54] A. C. Gadelha, A. R. Cadore, L. Lafeta, A. M. de Paula, L. M. Malard, R. G. Lacerda, L. C. Campos, *Nanotechnology* **2020**, *31*, 255701.
[55] D. Axelrod, D. E. Koppel, J. Schlessinger, E. Elson, W. W. Webb, *Biophys. J.* **1976**, *16*, 1055.
[56] J. Tønnesen, G. Katona, B. Rózsa, U. V. Nägerl, *Nat. Neurosci.* **2014**, *17*, 678.
[57] D. M. Kavanagh, A. M. Smyth, K. J. Martin, A. Dun, E. R. Brown, S. Gordon, K. J. Smillie, L. H. Chamberlain, R. S. Wilson, L. Yang, W. Lu, M. A. Cousin, C. Rickman, R. R. Duncan, *Nat. Commun.* **2014**, *5*, 5774.
[58] A. Chernikov, C. Ruppert, H. M. Hill, A. F. Rigosi, T. F. Heinz, *Nat. Photonics* **2015**, *9*, 466.
[59] J. He, D. He, Y. Wang, Q. Cui, F. Ceballos, H. Zhao, *Nanoscale* **2015**, *7*, 9526.
[60] D. R. Ceratti, Y. Rakita, L. Cremonesi, R. Tenne, V. Kalchenko, M. Elbaum, D. Oron, M. A. C. Potenza, G. Hodes, D. Cahen, *Adv. Mater.* **2018**, *30*, 1706273.
[61] D. Sustr, C. Duschl, D. Volodkin, *Eur. Polym. J.* **2015**, *68*, 665.
[62] Z. He, R. Zhao, X. Chen, H. Chen, Y. Zhu, H. Su, S. Huang, J. Xue, J. Dai, S. Cheng, M. Liu, X. Wang, Y. Chen, *ACS Appl. Mater. Interfaces* **2018**, *10*, 42524.
[63] Y. Guo, D. Sun, B. Ouyang, A. Raja, J. Song, T. F. Heinz, L. E. Brus, *Nano Lett.* **2015**, *15*, 5081.
[64] Y. Lee, S. J. Yun, Y. Kim, M. S. Kim, G. H. Han, A. K. Sood, J. Kim, *Nanoscale* **2017**, *9*, 2272.
[65] G. Danda, P. Masih Das, Y.-C. Chou, J. T. Mlack, W. M. Parkin, C. H. Naylor, K. Fujisawa, T. Zhang, L. B. Fulton, M. Terrones, A. T. C. Johnson, M. Drndić, *ACS Nano* **2017**, *11*, 1937.
[66] P. P. Jha, P. Guyot-Sionnest, *ACS Nano* **2009**, *3*, 1011.